



Insights from elastic thermobarometry into exhumation of high-pressure metamorphic rocks from Syros, Greece

Miguel Cisneros^{1,2*}, Jaime D. Barnes¹, Whitney M. Behr^{1,2}, Alissa J. Kotowski^{1,3*}, Daniel F. Stockli¹, and Konstantinos Soukis⁴

5 ¹Department of Geological Sciences, Jackson School of Geosciences, University of Texas at Austin, Austin, TX, USA

^{2*}Current address: Geological Institute, ETH Zürich, Zürich, Switzerland

^{3*}Current address: Department of Earth and Planetary Sciences, McGill, Montreal, Canada

⁴Faculty of Geology and Geoenvironment, NKUA, Athens, Greece

Correspondence to: Miguel Cisneros (miguel.cisneros@erdw.ethz.ch)

10 **Abstract.** We combine elastic thermobarometry with oxygen isotope thermometry to quantify the pressure-temperature (P-T) evolution of retrograde metamorphic rocks of the Cycladic Blueschist Unit (CBU), an exhumed subduction complex exposed on Syros, Greece. We employ quartz-in-garnet and quartz-in-epidote barometry to constrain pressures of garnet and epidote growth near peak subduction conditions and during exhumation, respectively. Oxygen isotope thermometry of quartz and calcite within boudin necks was used to estimate temperatures during exhumation and to refine pressure estimates. Three
15 distinct pressure groups are related to different metamorphic events and fabrics: high-pressure garnet growth at ~1.4 - 1.7 GPa between 500 - 550 °C, retrograde epidote growth at ~1.3 - 1.5 GPa between 400 - 500 °C, and a second stage of retrograde epidote growth at ~1.0 GPa and 400 °C. These results are consistent with different stages of deformation inferred from field and microstructural observations, recording prograde subduction to blueschist-eclogite facies and subsequent retrogression under blueschist-greenschist facies conditions. Our new results indicate that the CBU experienced cooling during
20 decompression after reaching maximum high-pressure/low-temperature conditions. These P-T conditions and structural observations are consistent with exhumation and cooling within the subduction channel in proximity to the refrigerating subducting plate, prior to Miocene core-complex formation. This study also illustrates the potential of using elastic thermobarometry in combination with structural and microstructural constraints, to better understand the P-T-deformation conditions of retrograde mineral growth in HP/LT metamorphic terranes.

25 1 Introduction

Constraining the pressure-temperature (P-T) evolution of metamorphic rocks is fundamental for understanding the mechanics, timescales, and thermal conditions of plate tectonic processes operating on Earth. Historically, one of the most challenging aspects of thermobarometry has been deciphering the P-T evolution of rocks during their exhumation from peak depths back to the surface (e.g., Kohn and Spear, 2000; Spear and Pattison, 2017; Spear and Selverstone, 1983). Exhumation
30 P-T paths are particularly challenging to reconstruct because during retrogression rocks are cooled, fluids are consumed by



metamorphic reactions, and strain is progressively localized, all of which result in more sluggish reaction kinetics and lesser degrees of chemical equilibrium (e.g., Baxter, 2003; Carlson, 2002; Jamtveit et al., 2016; Rubie, 1998). These issues are especially pronounced in high-pressure/low-temperature (HP/LT) environments characteristic of subduction zones.

Elastic thermobarometry offers an alternative to conventional thermobarometry. Rather than relying on equilibrium
35 metamorphic reactions, this approach constrains the P-T conditions at which a host crystal entraps an inclusion (e.g., Adams et al., 1975a, 1975b; Rosenfeld, 1969; Rosenfeld and Chase, 1961). Because inclusion-host-pair bulk moduli and thermal expansivities commonly differ, upon ascent, an inclusion develops residual strain(s) that can be determined from measurements of Raman shifts. A residual inclusion pressure can be calculated from strain(s) by using Grüneisen tensors (Angel et al., 2019; Murri et al., 2018, 2019) or experimental hydrostatic calibrations (e.g., Ashley et al., 2014; Enami et al., 2007; Thomas and
40 Spear, 2018). Elastic modeling is then used to calculate the initial entrapment conditions of when the host grew around the inclusion, and thus can be used to determine the conditions at which individual host minerals grew during metamorphism (e.g., Alvaro et al., 2020; Ashley et al., 2014a; Enami et al., 2007).

The purpose of this study is to illustrate the potential of using elastic thermobarometry in combination with structural and microstructural observations, to better understand the P-T-deformation (D) conditions of retrograde mineral growth in
45 subduction-related HP/LT metamorphic rocks. We focus on a subduction complex exposed on Syros Island, Cyclades, Greece, where despite several decades of petrological study, the early exhumation history remains enigmatic. We combine the recently tested quartz-in-epidote (qtz-in-ep) barometer (Cisneros et al., 2020), quartz-in-garnet (qtz-in-grt) barometry (e.g., Ashley et al., 2014; Bonazzi et al., 2019; Thomas and Spear, 2018), and oxygen isotope thermometry (e.g., Javoy, 1977; Urey, 1947), to constrain metamorphic growth pressures and temperatures near peak subduction depths and during early exhumation. The
50 results demonstrate that combining qtz-in-ep barometry with careful structural and microstructural observations allows us to delineate a retrograde P-T-D path that is contextually constrained, and is more robust than what is commonly possible with conventional thermobarometry.

2. Geologic Setting

Syros Island in the Cyclades of Greece consists of metamorphosed tectonic slices of oceanic and continental affinity
55 that belong to the Cycladic Blueschist Unit (CBU), structurally below the Pelagonian Upper Unit (Fig. 1). CBU rocks on Syros record Eocene subduction (~52 Ma) to peak blueschist-eclogite facies conditions (Lagos et al., 2007), followed by exhumation during Oligo-Miocene (~25 Ma) back-arc extension (e.g., Jolivet and Brun, 2010; Ring et al., 2010). A retrograde regional metamorphic event occurred between 25-18 Ma and caused greenschist- to amphibolite facies metamorphism in the Cycladic islands, but was most pervasive in the footwall adjacent to the large-scale extensional North and West Cycladic Detachment
60 Systems (e.g., Bröcker et al., 1993; Bröcker and Franz, 2006; Gautier et al., 1993; Grasemann et al., 2012; Jolivet et al., 2010; Pe-Piper and Piper, 2002; Schneider et al., 2018). Despite these documented metamorphic events, the exhumation history of



the CBU between ~52 and ~25 Ma remains enigmatic and poorly constrained; yet, this period spans exhumation of the CBU from maximum subduction to middle crust pressures (~0.3 - 0.7 GPa).

In this work focus on rocks within the CBU, which consist of intercalated metavolcanic and metasedimentary rocks, 65 metabasites, and serpentinites (e.g., Keiter et al., 2011). Conventional thermobarometry suggests that the CBU on Syros reached peak P-T conditions of ~1.5 GPa and ~500 °C (Ridley, 1984). Trotet et al. (2001a) and Laurent et al. (2018) suggest higher peak P-T conditions of ~2.0 - 2.4 GPa and ~500 - 550 °C; however, multi-mineral phase equilibria of marbles (Schumacher et al., 2008) and elastic thermobarometry of metabasites from Kini beach (Behr et al., 2018) support the original 70 P-T estimates of ~1.5 GPa and 500 °C. Published exhumation P-T paths for the CBU on Syros are also highly variable, ranging from cooling during decompression, near-isothermal decompression, to reheating during decompression (Laurent et al., 2018; Schumacher et al., 2008; Skelton et al., 2018; Trotet et al., 2001a). The range of previous P-T conditions reflects the lack of comprehensive studies that combine structural geology, petrology, and thermobarometry across the CBU. Because of these conflicting P-T paths, several models have been proposed to explain the exhumation history of the CBU, including coaxial 75 and extension (Lister and Forster, 2016; Trotet et al., 2001a, 2001b), and subduction channel exhumation (Laurent et al., 2016).

3. Field and Microstructural Observations

We studied four localities on Syros (Kalamisia, Delfini, Lotos, Megas Gialos; Fig. 1). Each locality exhibits multiple stages of mineral growth, and the same deformation and P-T progression. Kalamisia records blueschist facies metamorphism, and Delfini, Lotos, and Megas Gialos record blueschist-greenschist facies metamorphism. Localities of collected samples and 80 their associated mineralogy are provided in the supplementary material (Table S1).

3.1 Kalamisia

Mafic rocks from Kalamisia preserve retrograde blueschist facies metamorphism (Fig. 1). They exhibit an early foliation (S_s) characterized by relict blueschist and eclogite facies minerals. The early S_s fabric is re-folded by upright folds (F_{t1}) with steeply dipping axial planes, NE-SW-oriented fold hinge lines, and NE-SW-oriented stretching lineations primarily 85 defined by white mica, glaucophane, and epidote; this indicates folding under blueschist facies conditions (D_{t1}).

Garnets in Kalamisia mafic samples occur as ~1 - 4 mm porphyroblasts (KCS70A, Supplementary Fig. S1a), lack a well-defined internal foliation, and the S_s foliation deflect around garnets. Glaucophane typically grows within pressure shadows and brittle fractures of garnet, and omphacite displays breakdown and alteration to glaucophane; this indicates retrograde glaucophane growth. Glaucophane inclusions within epidote are commonly oriented parallel to S_s , and no omphacite 90 is observed as inclusions within epidote; these observations support epidote (ep1) growth during retrograde metamorphism.



3.2 Delfini Beach

Metasedimentary rocks at Delfini Beach show retrogression from eclogite- and blueschist- to greenschist facies (Fig. 1). The rocks at Delfini exhibit an early foliation (also considered S_s) characterized by relict blueschist and eclogite facies minerals (garnet porphyroblasts, and foliation-parallel white mica, blue amphibole, and epidote) aligned in tight isoclinal folds (F_s) with shallow axial planes. This early fabric was locally retrogressed and re-folded by upright folds (considered F_{t2}) with steeply dipping axial planes, E-W-oriented fold hinge lines, and E-W-oriented stretching lineations primarily defined by white mica, chlorite, and actinolite (considered D_{t2} , Fig. 2a,b); this indicates folding under greenschist facies conditions. D_{t2} folding was associated with boudinage of earlier-generation epidote parallel to the fold hinge lines, and simultaneous precipitation of new coarse-grained epidote (ep2), along with quartz, calcite and iron oxides in boudin necks (Fig. 3). In some areas of tight D_{t2} folding, a new generation of fine-grained epidote (also interpreted as ep2) grows within a newly developed crenulation cleavage (S_t , Fig. 2c,d,e).

Garnets in Delfini metasedimentary samples occur as ~1 - 4 mm, partially chloritized porphyroblasts (KCS34, Fig. 2c), and as <1 mm garnets that are commonly found as inclusions within epidote (KCS1621, Supplementary Fig. S1b). Foliation parallel epidotes (ep1) found within early blueschist-greenschist facies outcrops (KCS1621) range in size from ~0.5 - 5 mm (b-axis length), are strongly poikiloblastic, lack late greenschist facies inclusions such as chlorite, and commonly contain an internal foliation that is oblique to the external matrix S_s foliation (Fig. 2f,g; Supplementary Fig. S1b). Late epidote (ep2) crystals are found within sample KCS34 from the core of an upright fold (F_{t2}). During upright folding, a predominant portion of the rock is recrystallized to late-stage greenschist facies minerals, and contains new epidote (ep2) that is oriented parallel to the S_{t2} crenulation cleavage. Ep2 crystals range from ~50 - 300 μm along the b-axis (Fig. 2c,d,e), tend to be euhedral (Fig. 2d,e), sometimes contain titanite inclusions (Fig. 2d), and show textural equilibrium with white mica and titanite that also formed in the S_{t2} cleavage (Fig. 2d,e). Ep2 crystals are not poikiloblastic and rarely preserve quartz inclusions, thus only a few analyses were possible.

3.3 Lotos Beach

The rocks from Lotos Beach exhibit the same structural and petrological progression as those from Delfini (Fig. 1), showing retrogression from eclogite- and blueschist- to greenschist facies. An early S_s foliation was locally retrogressed and re-folded by upright F_{t2} folds with steeply dipping axial planes, E-W-oriented fold hinge lines, and E-W-oriented stretching lineations primarily defined by white mica, chlorite, and actinolite (D_{t2}). D_{t2} folding was associated with boudinage of earlier-generation epidote parallel to the fold hinge lines, and simultaneous precipitation of new coarse-grained epidote (ep2), along with quartz, calcite and iron oxides in boudin necks (Fig. 3).

Garnets in Lotos samples occur as ~1 - 3 mm chloritized porphyroblasts (e.g., KCS3), that deflect the external S_s foliation (KCS3). Foliation parallel epidotes (ep1) found within early blueschist-greenschist facies outcrops (SY1402, SY1405, KCS2, KCS3) range in size from ~0.5 - 5 mm (b-axis length), are strongly poikiloblastic, and commonly contain an internal



foliation that is oblique to the external matrix S_s foliation (Supplementary Fig. S1c). Boudinage of ep1 parallel to stretching lineations is common in thin sections (Supplementary Fig. S1c).

125 3.4 Megas Gialos

The rocks from Megas Gialos exhibit the same structural and petrological progression as those from Lotos and Delfini Beaches (Fig. 1). Rocks from Megas Gialos show retrogression from eclogite- and blueschist- to greenschist facies. An early S_s foliation was locally retrogressed and stretching lineations primarily defined by white mica, chlorite, and actinolite are E-W-oriented.

130 No garnets were found within the analyzed sample from Megas Gialos. Foliation parallel epidotes (ep1) found within early blueschist-greenschist facies outcrops range in size from $\sim 0.5 - 3$ mm (b-axis length), are strongly poikiloblastic, and commonly contain an internal foliation that is oblique to the external matrix S_s foliation (Supplementary Fig. S1d). Boudinage of ep1 parallel to stretching lineations is common in thin sections (Supplementary Fig. S1d).

4. Methods

135 We determined P-T conditions using elastic thermobarometry and oxygen isotope thermometry. Raman spectroscopy was used to measure Raman shifts of strained quartz inclusions entrapped within epidote or garnet, and a laser fluorination line and a GasBench II coupled to a gas source mass spectrometer was used to measure oxygen isotope ratios of quartz and calcite separates, respectively.

4.1 Raman Spectroscopy measurements

140 Our Raman spectroscopy measurements are taken from ~ 30 μm , ~ 80 μm , and ~ 150 μm thin and thick sections, that consist of sections cut perpendicular to foliation (S_s) and parallel to stretching lineations (e.g., KCS1621), and perpendicular to the F_{12} fold axial plane (KCS34). Quartz inclusions were measured from multiple epidotes and garnets within individual sections (Supplementary Table S3). Measured quartz inclusions were small in diameter relative to the host, and were two-to-three-times the inclusion radial distance from other inclusions, fractures, and the host exterior to avoid overpressures or stress relaxation (Fig. 4a,b; Campomenosi et al., 2018; Zhong et al., 2020). No geometric corrections were applied (Mazzucchelli et al., 2018).

150 Raman spectroscopy measurements of quartz inclusions within garnet and epidote were carried-out at Virginia Tech (VT) and ETH Zürich (ETHZ) by using JY Horiba LabRam HR800 and DILOR Labram Raman systems, respectively. Analyses at VT used an 1800 grooves mm^{-1} grating, 100x objective with a 0.9 numerical aperture (NA), 400 μm confocal aperture, and a 150 μm slit width. Raman spectra were centered at ~ 360 cm^{-1} . We used a 514.57 nm wavelength Ar laser, and removed the laser interference filter for all analyses to apply a linear drift correction dependent on the position of the 116.04 cm^{-1} , 266.29 cm^{-1} , and 520.30 cm^{-1} Ar plasma lines (Fig. DR4). Measurements at ETHZ used a 532 nm laser, an 1800 grooves



mm⁻¹ grating, a 100x objective with a 0.9 NA, a 200 μm confocal aperture, and a 300 μm slit width. Raman spectra were centered at ~ 850 cm⁻¹.

155 All Raman spectra was reduced with a Bose-Einstein temperature-dependent population factor (Kuzmany, 2009). All Raman bands were fit by using PeakFit v4.12 from SYSTAT Software Inc. A Gaussian model was used to fit Ar plasma lines (only VT analyses), and a Voigt model was used to fit the quartz 128 cm⁻¹, 206 cm⁻¹, and 464 cm⁻¹ bands, epidote bands, and garnet bands. Raman bands of quartz, epidote, and garnet, and Ar plasma lines were fit simultaneously, and a linear background subtraction was applied during peak fitting. Baseline-to-baseline deconvolution of quartz and garnet bands was simple and
160 generally required fitting quartz bands and a few shoulder garnet bands. Deconvolution of quartz and epidote bands required more complicated deconvolution; we followed a fitting approach similar to that described by Cisneros et al. (2020).

4.2 Inclusion and entrapment pressure calculations

The fully encapsulated inclusions preserve strain that causes the Raman active vibrational modes of inclusions to be shifted to higher or lower wavenumbers relative to minerals that are unstrained (fully exposed). We calculated the Raman
165 shift(s) of inclusions (ω_{inc}) relative to Raman shift(s) of an unencapsulated Herkimer quartz standard (ω_{ref}) at ambient conditions ($\Delta\omega = \omega_{inc} - \omega_{ref}$) (Fig. 4). For VT analyses, ω_{inc} was measured relative to a Herkimer quartz standard that was analyzed 5 times prior to same day analyses. A drift correction was applied to ω_{inc} by monitoring the position of Ar plasma lines (Supplementary Tables S2; S3). For ETHZ analyses, a Herkimer quartz standard was analyzed 3 times prior to and after quartz inclusion analyses. A time-dependent linear drift correction was applied to ω_{inc} based on the drift shown by Herkimer
170 quartz analyses that bracketed inclusion analyses (< 0.2 cm⁻¹).

We calculated residual inclusion pressures (P_{inc}) by using hydrostatic calibrations and by accounting for quartz anisotropy. To calculate a P_{inc} from individual quartz Raman bands, we used pressure-dependent Raman shift(s) ($P-\Delta\omega$) of the quartz 128 cm⁻¹, 206 cm⁻¹, and 464 cm⁻¹ bands, that have been experimentally calibrated under hydrostatic stress conditions by using diamond anvil cell experiments (Schmidt and Ziemann, 2000). To account for quartz anisotropy, we calculated P_{inc}
175 from strains. Calculating quartz strains requires that the Raman shift of at least 2 quartz vibrational modes can be measured. When we were able to measure the quartz 128, 206 and 464 cm⁻¹ band positions of inclusions, we calculated strains from the $\Delta\omega$ of 3 bands. If only two bands were measured, we calculated strains from the $\Delta\omega$ of 2 bands (Supplementary Table S3). For the remaining analyses with low 128 and 206 cm⁻¹ intensities, we report P_{inc} calculated from the 464 cm⁻¹ band hydrostatic $P-\Delta\omega$ relationship (Supplementary Table S3). Strains were determined from the $\Delta\omega$ of the 128 cm⁻¹, 206 cm⁻¹, and 464 cm⁻¹
180 quartz bands by using Strainman (Angel et al., 2019; Murri et al., 2018, 2019), wherein a weighted fit was applied based on the $\Delta\omega$ error associated with each quartz Raman band. Calculated strains were converted to a mean stress [$P_{inc} = (2\sigma_1 + \sigma_3)/3$] using the matrix relationship $\sigma_i = c_{ij}\epsilon_j$, where σ_i , c_{ij} , and ϵ_j , are the stress, elastic modulus, and strain matrices, respectively. We used the α -quartz trigonal symmetry constraints of Nye (1985) and quartz elastic constants of Wang et al. (2015).

We assumed constant mineral compositions for all modeling (epidote: $X_{ep} = 0.5$ and $X_{cz} = 0.5$; garnet: $X_{Alm} = 0.7$,
185 $X_{Gr} = 0.2$, and $X_{Py} = 0.1$). Garnet compositions have a negligible effect on entrapment pressures (P_{trap}) because the



thermodynamic and physical properties of garnet end-members are similar (e.g., Supplementary Table S8); however, epidote composition has a greater effect on P_{trap} (Cisneros et al., 2020). To account for epidote and garnet solid solutions, we implemented linear mixing of shear moduli and molar volumes (V). Ideal mixing of molar volumes has been shown to be an appropriate approximation for epidote-clinzoisite solid solutions (Cisneros et al., 2020; Franz and Liebscher, 2004). Garnet molar volumes were modeled using the thermodynamic properties of Holland and Powell (2011) (almandine and pyrope) and Milani et al. (2017) (grossular), and a Tait Equation of State (EoS) with a thermal pressure term. We used the shear moduli of Wang and Ji (2001) (almandine and pyrope) and Isaak et al. (1992) (grossular). Epidote molar volumes were modeled using the thermodynamic properties and shear moduli given by Cisneros et al. (2020), and a Tait EoS and thermal pressure term. Epidote and clinzoisite regressions are based on the P-V-T data of Gatta et al. (2011) ($X_{\text{ep}} = 0.74$), and T-V and P-V data of Pawley et al. (1996) ($X_{\text{ep}} = 0$) and Qin et al. (2016) ($X_{\text{ep}} = 0.39$), respectively. Clinzoisite and epidote have similar thermal expansivities but differing bulk moduli (Supplementary Table S4). To account for the composition of epidotes used in P-V-T experiments, we normalized the composition of our unknown epidotes across the compositional range of P-V experimental epidotes, i.e., the molar volume of our unknown epidote ($X_{\text{ep}} = 0.5$) is estimated as 31 % ($X_{\text{ep}} = 0.74$) and 69 % ($X_{\text{ep}} = 0.39$) of each experimental epidote. Quartz molar volumes were modeled using the thermodynamic properties and approach of Angel et al. (2017a). Entrapment pressures were calculated from residual quartz P_{inc} by using the Angel et al. (2017b) 1D elastic model equation, and a MATLAB program available in Cisneros and Befus (2020) that implements mixing of shear moduli and molar volumes. A comparison of entrapment pressures calculated from the Cisneros and Befus (2020) MATLAB program and EoSFit-Pinc (Angel et al., 2017b) is given in Supplementary Table S4; entrapment pressure calculations of mineral end-members accounts for the reproducibility of molar volume and elastic modeling calculations.

205 4.3 Stable isotope measurements

Samples were measured by using a ThermoElectron MAT 253 isotope ratio mass spectrometer (IRMS) at the University of Texas at Austin. Quartz $\delta^{18}\text{O}$ values were measured by laser fluorination (Sharp, 1990), and ~2.0 mg of quartz were used in each analysis. Quartz from samples SY1613, SY1617, and SY1623 was duplicated to determine isotopic homogeneity and reproducibility. An internal quartz Lausanne-1 standard ($\delta^{18}\text{O} = +18.1\text{‰}$) was analyzed with all samples to evaluate precision and accuracy. All $\delta^{18}\text{O}$ values are reported relative to standard mean ocean water (SMOW), where the $\delta^{18}\text{O}$ value of NBS-28 is +9.65‰. Measurement precision based on the long-term reproducibility of standards is $\pm 0.1 \text{‰}$ (1 σ). Precision of Lausanne-1 on the day of analysis was $\pm 0.3 \text{‰}$ (1 σ), whereas samples reproduced with a precision of $\pm 0.1 \text{‰}$ (1 σ) or better (Supplementary Table S5). Calcite $\delta^{18}\text{O}$ values were measured on a Thermo Gasbench II coupled to a ThermoElectron 253 mass spectrometer. Each analysis used 0.25 - 0.5 mg of calcite that was loaded into Exetainer vials, flushed with ultra-high purity helium, and reacted with 103 % phosphoric acid at 50 °C for ~2 hours. Headspace CO_2 was then transferred to the mass spectrometer. Samples were calibrated to an in-house standard, NBS-18, and NBS-19. Measurement precision is $\pm 0.04 \text{‰}$ (1 σ) based on the long-term reproducibility of standards.



4.4 Stable isotope temperature calculations

220 Temperatures derived from stable isotope measurements were calculated by using the Sharp and Kirschner (1994) quartz-calcite oxygen isotope fractionation calibration ($A = 0.87 \pm 0.06$; equation A1; Supplementary Table S5). Isotopic equilibrium was assumed for all samples. Several observations support that this assumption is appropriate: 1) duplicate $\delta^{18}\text{O}$ analysis of quartz and calcite grains give the same isotopic value, suggesting grain isotopic homogeneity, 2) the stage of deformation that these mineral pairs are related to is not affected by further deformation in either outcrop or thin section, and 3) all quartz-calcite pairs suggest a similar temperature of isotopic equilibration.

225 Temperature errors from quartz-calcite oxygen isotope measurements were calculated through the square-root of the summed quadratures of all sources of uncertainty (equations A2, A3). These uncertainties included $\delta^{18}\text{O}$ value errors of quartz and calcite of $\pm 0.1 \text{ ‰}$ (1σ) and $\pm 0.04 \text{ ‰}$ (1σ), respectively, and errors associated with the Sharp and Kirschner (1994) quartz-calcite oxygen isotope fractionation calibration (A parameter).

4.5 Electron probe measurements

230 Electron probe analyses were carried-out at ETHZ using a JEOL JXA-8230 Electron Probe Microanalyzer (EPMA). The EPMA is equipped with five wavelength-dispersive spectrometers. Epidote and omphacite were analyzed for Si Al, Na, Mg, Ca, Cr K, Ti, Fe, and Mn on TAP, TAPH, PETJ, PETL, and LIFH crystals. Beam parameters included a 20 nA beam current, 10 μm beam size, and a 15 keV accelerating voltage. All elements were measured for 30 s on peak and a mean atomic number background correction was applied. Primary standards used included: albite, anorthite, synthetic forsterite, chromite, 235 microcline, synthetic rutile, synthetic fayalite, and synthetic pyrolysite.

5. Results

Determined pressures were categorized into three groups according to outcrop and microstructural context (Fig. 5; Fig. 6; Supplementary Table S3): garnet growth near peak metamorphic conditions (Group 1), growth of foliation-parallel epidote during blueschist-greenschist facies metamorphism (ep1, Group 2), and late-stage epidote growth in the new 240 crenulation (S_{l2}) associated with F_{l2} folds during greenschist facies metamorphism (ep2, Group 3). New ep2 growth is also supported by the mineral chemistry of different epidote generations within the S_{l2} crenulation. Epidotes show a progressive chemical evolution that is recorded by an early generation epidote inclusion in titanite that occurs parallel to S_{l2} ($X_{\text{ep}} \cong 0.1$), the ep2 core ($X_{\text{ep}} \cong 0.5$), and the ep2 rim ($X_{\text{ep}} \cong 0.8$) (Fig. 2g; Supplementary Table S6).

245 The entrapment temperature (T_{trap}) of quartz inclusions in garnet (garnet growth temperature) is estimated as 500 - 550 $^{\circ}\text{C}$; this is based on good agreement between previous studies on the maximum temperature reached by CBU rocks from Syros (e.g., Laurent et al., 2018; Ridley, 1984; Schumacher et al., 2008; Skelton et al., 2018; Trotet et al., 2001a). T_{trap} for the ep2 population (Group 3) is deduced from oxygen isotope thermometry of quartz-calcite boudin-neck precipitates. The mean temperature from quartz-calcite pairs from boudin necks is $411 \pm 23 \text{ }^{\circ}\text{C}$ ($n = 4$, Supplementary Table S5). T_{trap} for the ep1



250 population (Group 2) is estimated as being intermediate between garnet and ep2 growth (~400 - 500 °C). As shown by qtz-in-
ep isomekes (constant P_{inc} lines along which fractional volume changes of an inclusion and host are equal), the assumed T_{trap}
has a minimal effect on P_{trap} (Fig. 6b; Cisneros et al., 2020).

5.1 Kalamisia

255 Group 1 quartz-inclusions-in-garnet record a mean P_{inc} of 600 ± 78 MPa (Fig 4; Supplementary Table S3). This
corresponds to an entrapment pressure (P_{trap}) of $1.43 - 1.49 \pm 0.14$ GPa ($n = 5$), at an estimated T_{trap} between 500 - 550 °C (Fig.
6b, Supplementary Table S3). Group 2 quartz-inclusions-in-ep1 record a mean P_{inc} of 544 ± 57 MPa, corresponding to a P_{trap}
of 1.43 ± 0.12 ($n = 6$) at an estimated T_{trap} of 450 °C. No Group 3 epidotes are found within our analyzed section from
Kalamisia.

5.2 Delfini

260 Group 1 records a mean P_{inc} of 739 ± 49 MPa (Fig 4; Supplementary Table S3). This corresponds to a P_{trap} of 1.68 -
 1.74 ± 0.09 GPa ($n = 20$), at an estimated T_{trap} between 500 - 550 °C (Fig. 6b, Supplementary Table S3). Group 2 records a
mean P_{inc} of 518 ± 52 MPa, corresponding to a P_{trap} of 1.38 ± 0.11 ($n = 5$) at an estimated T_{trap} of 450 °C. Group 3 records a
mean P_{inc} of 343 ± 23 MPa, corresponding to a P_{trap} of 0.98 ± 0.05 GPa ($n = 3$) at 411 °C (Supplementary Table S3).

5.3 Lotos

265 Group 1 records a mean P_{inc} of 751 ± 76 MPa (Fig 4; Supplementary Table S3). This corresponds to a P_{trap} of 1.70 -
 1.76 ± 0.14 GPa ($n = 2$), at an estimated T_{trap} between 500 - 550 °C (Fig. 6b; Supplementary Table S3). Group 2 records a
mean P_{inc} of 531 ± 78 MPa, corresponding to a P_{trap} of 1.41 ± 0.17 ($n = 15$) at an estimated T_{trap} of 450 °C. No Group 3 epidotes
were analyzed from Lotos.

5.4 Megas Gialos

270 Group 2 records an average P_{inc} of 494 ± 29 MPa (Fig. 6), corresponding to a P_{trap} of 1.33 ± 0.03 ($n = 6$) at an estimated
 T_{trap} of 450 °C (Fig. 6b; Supplementary Table S3). No Group 1 garnets or Group 3 epidotes were analyzed from Megas Gialos.

6. Discussion

6.1 Elastic thermobarometry pressure groups

275 Group 1 garnets either lack an internal foliation or contain a weak foliation that is defined by inclusions oblique to
the S_s fabric, which indicates a previous stage of deformation (Fig. 2c; Supplementary Fig. S1a,b). Garnets record similar
pressures, regardless of the location of quartz inclusions (Supplementary Table S3). Omphacite inclusions within different



garnet zones also show no difference in composition, which is consistent with qtz-in-grt barometry results (Delfini: KCS1621, Supplementary Table S5). Group 2 epidotes (ep1) overgrow garnets, are aligned parallel to the S_s foliation but sometimes preserve an internal foliation that is oblique to S_s , and lack late greenschist facies inclusions (Fig. 2f,g; Supplementary Fig. S1). Group 3 epidotes (ep2, KCS34, Fig. 2c,d,e) are short in length, are aligned parallel to a late S_{l2} crenulation, contain
280 minimal quartz inclusions, and only record Group 3 pressures, independent of the position of quartz inclusions within epidotes.

Based on these observations, the Group 1 P_{trap} estimates from the qtz-in-grt barometer record high-P conditions on Syros associated with prograde garnet growth, and the Group 2 and 3 P_{trap} estimates from the qtz-in-ep barometer record epidote growth during early blueschist-greenschist facies retrogression (ep1, D_{t1}) and subsequent D_{l2} deformation (ep2), respectively. We interpret the low-P epidote group (Group 3) to be associated with D_{l2} folding, and best recorded in areas that experienced
285 late greenschist facies mineral growth due to enhanced deformation and/or fluid influx during this stage of deformation (e.g., core of F_{l2} fold).

6.2 Comparison of peak pressure constraints for the CBU on Syros and Sifnos

Based on qtz-in-grt measurements (Group 1), our P_{trap} calculations suggest maximum P conditions of $\sim 1.6 - 1.8$ GPa were reached by the CBU on Syros. Garnets from metasedimentary and metavolcanic rocks record the statistically highest P_{trap}
290 ($\sim 1.5 - 1.8$ GPa), whereas garnets from metamafic rocks (Kalamisia) record the lowest P_{trap} ($\sim 1.3 - 1.6$ GPa) (Fig. 6b). We present a compilation of previous P-T constraints on CBU rocks from Syros and Sifnos, Greece, and discuss how our P_{trap} constraints compare with previous studies.

Elastic thermobarometry, mineral stability constraints, and multi-phase equilibrium modeling results from Sifnos CBU rocks suggest maximum P conditions of $\sim 1.8 \pm 0.1$ GPa (Ashley et al., 2014), $\sim 1.4 \pm 0.2$ GPa (Matthews and Schliestedt,
295 1984), and $\sim 2.0 - 2.2$ GPa (Dragovic et al., 2012, 2015; Groppo et al., 2009; Trotet et al., 2001a), respectively. The results of Ashley et al. (2014) are commonly cited as evidence that the CBU reached high pressure conditions (≥ 2.0 GPa, from elastic thermobarometry); however, their P_{trap} calculations were carried out by using fits to quartz molar volume (P-T-V) data that have recently been re-evaluated (Angel et al., 2017a). Improved fits to quartz molar volume experiments “soften” quartz, and remodeling P_{inc} values from Ashley et al. (2014) reduces maximum mean P_{trap} conditions to $\sim 1.6 \pm 0.1$ GPa (Fig. 6a,
300 Supplementary Table S7).

Elastic thermobarometry, mineral stability constraints, glaucophane-bearing marble mineral equilibria, and multi-phase equilibria modeling results from Syros CBU rocks suggest peak pressure conditions of $\sim 1.5 \pm 0.1$ GPa (Behr et al.,
2018), $\sim 1.4 - 1.9$ GPa (Ridley, 1984), ~ 1.5 GPa (Schumacher et al., 2008), and $\sim 1.9 - 2.4$ GPa (Laurent et al., 2018; Skelton et al., 2018; Trotet et al., 2001a), respectively. Elastic thermobarometry results from Syros, Greece were reduced using the
305 approach outlined in (Ashley et al., 2016), wherein a correction to P_{trap} is applied based on the assumed T_{trap} . Recent studies suggest that not using a temperature-dependent P_{trap} correction produces suitable results that accurately reproduce experimental conditions of quartz entrapment by garnet (Bonazzi et al., 2019; Thomas and Spear, 2018). Recalculation of the Behr et al. (2018) P_{inc} data (no temperature-dependent P_{trap} correction) results in a mean P_{trap} of $\sim 1.7 \pm 0.1$ GPa (Fig. 6a, Supplementary



310 Table S8). The re-evaluation of data from Ashley et al. (2014) and Behr et al. (2018) suggests that our results are in good agreement with previous elastic thermobarometry constraints, and that to date, no qtz-in-grt elastic thermobarometry results suggest pressures ≥ 2.0 GPa.

Different methodologies applied to CBU rocks from Syros have resulted in a wide range of maximum P estimates. Schumacher et al. (2008) used mineral-equilibria modeling of glaucophane-bearing marbles to place constraints on maximum P-T conditions. Maximum P-T conditions are constrained by the presence of glaucophane + CaCO₃ + dolomite + quartz, which
315 suggests that the marbles exceeded the albite/Na-pyroxene + dolomite + quartz \rightarrow glaucophane + CaCO₃ reaction, but did not cross the dolomite + quartz \rightarrow tremolite + CaCO₃ or the glaucophane + aragonite-out reactions. The mineral reaction constraints suggest maximum P-T conditions of $\sim 1.5 - 1.6$ GPa and 500 °C for the CBU marbles. Ridley (1984) used the stability of paragonite and lack of kyanite to deduce max P constraints of $\sim 1.4 - 1.9$ GPa. Trotet et al. (2001b, 2001a), Laurent et al. (2018), and Skelton et al. (2018) employed thermodynamic phase-equilibria modeling and supplementary methods to
320 constrain P-T conditions for CBU rocks from Syros. Skelton et al. (2018) used the Powell and Holland (1994) Thermocalc database, Trotet et al. (2001b, 2001a) used the Berman (1991) thermodynamic database and the TWEEQC approach, and Laurent et al. (2018) used empirical thermobarometry, GrtMod (Lanari et al., 2017), and isochemical phase diagrams. Trotet et al. (2001b, 2001a), Laurent et al. (2018), and Skelton et al. (2018) found high-P conditions for the CBU (≥ 1.9 GPa), and results from Laurent et al. (2018) suggest some rocks reached conditions as high as 2.4 GPa. Results from Laurent et al. (2018)
325 suggest most garnet growth occurred at ~ 1.8 GPa and 500 °C; however, some garnet modeling results suggest that garnet rims grew at ~ 2.4 GPa and 500 - 550 °C, albeit errors are increasingly large for these results ($\pm 0.4 - 0.9$ GPa).

Some GrtMod results suggest prograde core and rim garnet growth at ~ 1.8 GPa and 475 °C, and ~ 2.4 GPa and 475 °C, respectively (sample SY1418 from; Laurent et al., 2018). These results would indicate that the garnets grew under isothermal conditions during prograde subduction, a result that we find difficult to reconcile within a subduction zone
330 geothermal gradient. Garnet results from another sample (SY1401) suggest core and rim garnet growth at ~ 1.8 GPa and 475 °C, and ~ 2.4 GPa and 550 °C, respectively. Sample SY1401 is collected from the same locality as ours (Kalamisia), but our qtz-in-grt results from this study suggest that garnets from this outcrop record the statistically lowest P_{trap} . It is possible, however, that we did not sample the same rocks as Laurent et al. (2018), or that we have not found or analyzed garnets that record high pressures.

335 Previous studies have also suggested that pressures ≥ 2.0 GPa are unreasonable for Syros because paragonite is abundant in CBU rocks, but kyanite has not been reported. This suggests that CBU rocks did not cross the reaction paragonite \rightarrow jadeite₅₀ + kyanite + H₂O ($\sim 1.9 - 2.0$ GPa); however, we recognize that the occurrence of kyanite may require high Al₂O₃:SiO₂ ratios for metabasites (e.g., Liati and Seidel, 1996), and that the pressure of this reaction is compositionally dependent. Pseudosections of eclogite CBU rocks show that kyanite would not be found in these bulk compositions below
340 ~ 2.3 GPa (Skelton et al., 2018). It is possible that the high-P conditions found in previous studies may be real, but may only be recorded locally within some eclogite blocks.



In general, phase stability relationships (e.g., Matthews and Schliestedt, 1984; Ridley, 1984; Schumacher et al., 2008) and qtz-in-grt barometry results are in good agreement, but do not agree with high-pressure results (≥ 1.9 GPa) deduced from thermodynamic modeling using approaches such as GrtMod and TWEEQC. The difference between our results and those of previous studies is important to reconcile, because the maximum P conditions reached by the CBU has considerable implications for the internal architecture of the CBU, its geodynamic evolution, and the mechanisms that can accommodate exhumation mechanisms of high-P subduction zone rocks from Syros. A comparison of qtz-in-grt barometry with thermodynamic modeling results from samples that record high pressures would be appropriate for further testing differences between the two techniques.

350 6.3 Comparison of exhumation P-T conditions

Previous studies have presented varying P-T paths and associated exhumation histories for Syros CBU rocks (Fig. 6a; Laurent et al., 2018; Schumacher et al., 2008; Skelton et al., 2018; Trotet et al., 2001a). We present a compilation of previous P-T constraints and interpretations and discuss how our results compare with previous studies.

Schumacher et al. (2008) do not provide quantitative constraints for the retrograde P-T path (schematic), and samples do not have structural context; however, the authors suggest that a “cold” P-T path during exhumation is required for Syros CBU rocks based on the occurrence of lawsonite + epidote assemblages across Syros, and the P-T path required to avoid crossing the lawsonite \rightarrow kyanite + zoisite reaction (Fig. 6a). The authors suggest that exhumation of CBU packages occurred shortly after juxtaposition near peak metamorphic conditions.

Both Trotet et al. (2001a, 2001b) and Laurent et al. (2018) constrain high-P conditions for the CBU (> 2.0 GPa), however, their proposed exhumation histories differ. Trotet et al. (2001b) suggested that CBU eclogites, blueschists and greenschists underwent different T-t histories during exhumation and were juxtaposed late along ductile shear zones. Laurent et al. (2018) suggested that the entire CBU reached peak metamorphic conditions of ~ 2.2 GPa, and that units that preserved blueschist facies assemblages underwent cooling during decompression, whereas rocks of southern Syros from lower structural levels experienced isobaric heating (~ 550 °C) at mid-crustal depths (~ 1.0 GPa) followed by subsequent cooling. Laurent et al. (2018) interpreted reheating to indicate that CBU rocks on Syros reached high-P conditions, and then rapidly transitioned from a forearc to back-arc setting, thus experiencing a period of increasing temperatures.

Skelton et al. (2018) also estimated peak and exhumation P-T conditions of rocks from Fabrikas (southern Syros), and interpreted exhumation of the CBU within an extrusion wedge (Ring et al., 2020). The authors constrained maximum P-T conditions of ~ 1.9 GPa and 525 °C, and retrograde conditions of ~ 1.4 GPa and 500 °C (blueschist facies) and ~ 0.3 GPa and 450 °C (greenschist facies) based on Thermocalc end-member activity modeling (Powell and Holland, 1994). Retrograde blueschist conditions (inferred from garnet growth) are similar between their estimates and ours, but greenschist facies conditions vastly differ. However, Skelton et al. (2018) focused on greenschist facies outcrops wherein metamorphism occurred locally over short length scales (e.g. $\sim 10 - 100$ m), adjacent to late-stage brittle normal faults. We interpret our D_2 stage of greenschist facies metamorphism to pre-date late-stage normal faulting that has been attributed to Neogene block



375 rotations (Cooperdock and Stockli, 2016) or possible coeval granitoid magmatism during Miocene back-arc extension (Keiter
et al., 2011).

Our results show that rocks from Kalamisia, Delfini, Lotos, and Megas Gialos, reached peak P-T conditions and
underwent cooling during retrograde blueschist and greenschist facies metamorphism (Fig. 6b). Peak P-T conditions of the
CBU are $\sim 1.6 - 1.8$ GPa and $500 - 550$ °C (Group 1 qtz-in-grt P_{trap} estimates), indicating a subduction zone geothermal gradient
380 of $\sim 9 - 10$ °C km^{-1} at $\sim 55 - 60$ km (assuming 30 MPa km^{-1}). Group 2 and 3 qtz-in-ep P_{trap} estimates indicate geothermal gradients
of ~ 10 °C km^{-1} and ~ 12 °C km^{-1} at ~ 47 and 33 km depths, respectively (Fig. 6b), demonstrating a similar P-T trajectory during
exhumation. Our P-T constraints are inconsistent with reheating to ~ 550 °C and 1.0 GPa, wherein amphibolite facies
mineralogy may be stable. Our samples and the sample from which Laurent et al. (2018) determined reheating (SY1407),
385 preserve no mineralogical evidence for having reached epidote-amphibolite facies (Fig. 6a; e.g., pargasite/hornblende,
biotite/muscovite). Instead, the matrix mineralogy of sample SY1407 (glaucofane, phengite, rutile) suggests that these rocks
formed under a cold geothermal gradient, rather than in a back-arc setting with an elevated geothermal gradient. Laurent et al.
(2018) suggest that sample SY1407 records albite-epidote-blueschist conditions, a field metamorphic facies that can expand
to higher T conditions; however, a pseudosection created for a similar bulk composition suggests that the determined P-T
constraints (~ 1.0 GPa and 550 °C) are within epidote-amphibolite facies (Trotet et al., 2001a). Furthermore, results from
390 sample SY1407 of Laurent et al. (2018) significantly disagree when using local vs. bulk compositions for modeling. Models
that use bulk compositions suggest that the core and mantle of the garnet record P-T conditions ~ 1.8 GPa and 475 °C, whereas
models that use local compositions suggest that the garnets do not record conditions above ~ 1.0 GPa. Lanari and Engi (2017)
have documented this issue, and describe how implemented compositions can drastically affect calculated P-T conditions; it
remains unclear how much the chosen bulk composition alters the P-T constraints of Laurent et al. (2018) for sample SY1407.

395 Our results suggest that rocks from different Syros outcrops record similar peak and exhumation P-T conditions, but
experienced different extents of deformation and thus recrystallization during exhumation. The similar peak pressures between
different Syros outcrops suggests that these rocks belong to what has been called the “Upper Cycladic Blueschist Nappe” on
Milos Island (as opposed to the “Lower Cycladic Blueschist Nappe”), which records peak pressure conditions above ~ 0.8 GPa
(Grasemann et al., 2018). The observation of similar P-T conditions reached at different locations is inconsistent with results
400 that suggest individual P-T paths for rocks that preserve different metamorphic facies (Trotet et al., 2001b, 2001a), and
different sections of the CBU (Laurent et al., 2018); however, we do not have T constraints for rocks from southern Syros. Our
results are in better agreement with a P-T evolution resembling that of Schumacher et al. (2008), and a geothermal gradient of
 $\sim 10 - 12$ °C km^{-1} that has also been proposed for CBU rocks from Sifnos, Greece (Schmädicke and Will, 2003).

6.4 Implications for exhumation mechanisms

405 Our results indicate that the CBU followed a “cooling during decompression” P-T trajectory that required a heat sink
at depth to cool rocks during exhumation. Cooling could be achieved under a steady-state subduction zone thermal gradient
with slab-top temperatures similar to those of warm subduction zones, such as in Cascadia (e.g., Syracuse et al., 2010;



Walowski et al., 2015). This would suggest that exhumation was achieved parallel to the subducting plate, in a subduction channel geometry prior to core-complex formation. During this phase of exhumation, CBU rocks remained within a cold forearc until they reached the mid-crust (~1.0 GPa), and exhibit a progressive change in kinematics, from N-S stretching lineations during subduction (Behr et al., 2018), to lineations that swing towards the E-W during exhumation (c.f., Kotowski and Behr, 2019; Laurent et al., 2016). The inferred P-T conditions and kinematics of our studied samples are consistent with Syros recording early deformation and metamorphism within a forearc setting, whereas adjacent Cycladic islands that border the North and West Cycladic Detachment Systems record late-stage kinematics and greenschist facies metamorphism that capture the CBU transition to a warmer back-arc setting.

7. Conclusions

This work highlights the potential of using elastic thermobarometry in combination with structural (macro and micro) and petrographic constraints, to better constrain P-T conditions of challenging rock assemblages. Our results allow us to place robust P-T constraints on distinct textural fabrics that are related to well-constrained outcrop scale structures. In particular, the work highlights how the qtz-in-ep barometer is well suited for constraining formation conditions of epidote, a common mineral that is found within a large range of geologic settings and P-T conditions. Combining the qtz-in-ep barometer with other elastic thermobarometers (e.g., qtz-in-grt) allows determination of protracted P-T histories from minerals that record different geologic stages within single rocks samples.

Our new results show that CBU rocks from Syros, Greece, experienced similar P-T conditions during subduction and exhumation, inconsistent with results that suggest different P-T histories for CBU rocks for Syros or increasing temperatures during exhumation. Our targeted stages of deformation and metamorphism suggest that CBU rocks from Syros record cooling during decompression, consistent with exhumation within a subduction channel and early deformation and metamorphism within a forearc (at least to ~33 km depth), prior to Miocene core-complex formation and transition to a warmer back-arc setting.

Appendix A: Stable isotope temperature error calculations

Temperature errors from oxygen isotope measurements were calculated through the square-root of the summed quadratures of all sources of uncertainty. These uncertainties included error of $\delta^{18}\text{O}$ values of quartz (qtz) and calcite (cc) of $\pm 0.1\text{‰}$ (1σ) and $\pm 0.04\text{‰}$ (1σ), respectively, and errors associated with the Sharp and Kirschner (1994) quartz-calcite oxygen isotope fractionation calibration (A parameter). Errors from the sum of propagated analytical errors, were propagated through the empirical calibration of quartz-calcite oxygen isotope fraction that was used for temperature calculations:

$$\Delta_{qtz-cc} = \frac{A \times 10^6}{T^2} \quad A1$$



where $A = 0.87 \pm 0.06$ (1σ). The square-root of the summed quadratures is expressed as:

$$\sigma_T = \sqrt{\sigma_A^2 \left(\frac{\partial T}{\partial A}\right)^2 + \sigma_{\Delta_{qtz-cc}}^2 \left(\frac{\partial T}{\partial \Delta_{qtz-cc}}\right)^2} \quad A2$$

440

$$\sigma_T = \sqrt{\sigma_A^2 \left(\frac{0.5 * 10^3}{\sqrt{A} * \sqrt{\Delta_{qtz-cc}}}\right)^2 + \sigma_{\Delta_{qtz-cc}}^2 \left(-0.5 * \frac{\sqrt{A} * 10^3}{\Delta_{qtz-cc}^{1.5}}\right)^2} \quad A3$$

Author Contribution

All authors contributed to this manuscript. M. Cisneros developed the epidote barometer, collected the data, and wrote the manuscript. J. Barnes, W. Behr, A. Kotowski, D. Stockli, and K. Soukis helped with conceiving the project, field work, and writing.

445

Acknowledgements

We thank N. Raia for field work assistance, J. Allaz for assistance on the microprobe at ETH Zürich, and C. Farley and R. Bobnar for access to the Raman Spectrometer at Virginia Tech. This work was supported by a GSA Student Research Grant and a Ford Foundation Fellowship awarded to M.C., an NSF Graduate Research Fellowship awarded to A.K., and NSF Grant (EAR-1725110) awarded to J.B., W.B., and D.S.

450

References

- Adams, H. G., Cohen, L. H. and Rosenfeld, J. L.: Solid inclusion piezothermometry I: comparison dilatometry, *American Mineralogist*, 60, 574–583, 1975a.
- Adams, H. G., Cohen, L. H. and Rosenfeld, J. L.: Solid inclusion piezothermometry II: geometric basis, calibration for the association quartz-garnet, and application to some pelitic schists, *American Mineralogist*, 60, 584–598, 1975b.
- Alvaro, M., Mazzucchelli, M. L., Angel, R. J., Murri, M., Campomenosi, N., Scambelluri, M., Nestola, F., Korsakov, A., Tomilenko, A. A., Marone, F. and Morana, M.: Fossil subduction recorded by quartz from the coesite stability field, *Geology*, 48(1), 24–28, doi:10.1130/G46617.1, 2020.



- 460 Angel, R. J., Alvaro, M., Miletich, R. and Nestola, F.: A simple and generalised P-T-V EoS for continuous phase transitions, implemented in EosFit and applied to quartz, *Contrib Mineral Petrol*, 172(5), 29, doi:10.1007/s00410-017-1349-x, 2017a.
- Angel, R. J., Mazzucchelli, M. L., Alvaro, M. and Nestola, F.: EosFit-Pinc: A simple GUI for host-inclusion elastic thermobarometry, *American Mineralogist*, 102(9), 1957–1960, doi:http://dx.doi.org/10.2138/am-2017-6190, 2017b.
- Angel, R. J., Murri, M., Mihailova, B. and Alvaro, M.: Stress, strain and Raman shifts, *Zeitschrift für Kristallographie - Crystalline Materials*, 234(2), 129–140, doi:10.1515/zkri-2018-2112, 2019.
- 465 Ashley, K. T., Caddick, M. J., Steele-MacInnis, M. J., Bodnar, R. J. and Dragovic, B.: Geothermobarometric history of subduction recorded by quartz inclusions in garnet, *Geochemistry, Geophysics, Geosystems*, 15(2), 350–360, doi:10.1002/2013GC005106, 2014.
- Ashley, K. T., Steele-MacInnis, M., Bodnar, R. J. and Darling, R. S.: Quartz-in-garnet inclusion barometry under fire: Reducing uncertainty from model estimates, *Geology*, 44(9), 699–702, doi:10.1130/G38211.1, 2016.
- 470 Baxter, E. F.: Natural constraints on metamorphic reaction rates, Geological Society, London, Special Publications, 220(1), 183–202, doi:10.1144/GSL.SP.2003.220.01.11, 2003.
- Behr, W. M., Kotowski, A. J. and Ashley, K. T.: Dehydration-induced rheological heterogeneity and the deep tremor source in warm subduction zones, *Geology*, 46(5), 475–478, doi:10.1130/G40105.1, 2018.
- 475 Berman, R. G.: Thermobarometry using multi-equilibrium calculations; a new technique, with petrological applications, *The Canadian Mineralogist*, 29(4), 833–855, 1991.
- Bonazzi, M., Tumiatei, S., Thomas, J., Angel, R. J. and Alvaro, M.: Assessment of the reliability of elastic geobarometry with quartz inclusions, *Lithos*, 105201, doi:10.1016/j.lithos.2019.105201, 2019.
- Bröcker, M. and Franz, L.: Dating metamorphism and tectonic juxtaposition on Andros Island (Cyclades, Greece): results of a Rb–Sr study, *Geological Magazine*, 143(5), 609–620, doi:10.1017/S001675680600241X, 2006.
- 480 Bröcker, M., Kreuzer, H., Matthews, A. and Okrusch, M.: ⁴⁰Ar/³⁹Ar and oxygen isotope studies of polymetamorphism from Tinos Island, Cycladic blueschist belt, Greece, *Journal of Metamorphic Geology*, 11(2), 223–240, doi:10.1111/j.1525-1314.1993.tb00144.x, 1993.
- Campomenosi, N., Mazzucchelli, M. L., Mihailova, B., Scambelluri, M., Angel, R. J., Nestola, F., Reali, A. and Alvaro, M.: How geometry and anisotropy affect residual strain in host-inclusion systems: Coupling experimental and numerical approaches, *American Mineralogist*, 103(12), 2032–2035, doi:10.2138/am-2018-6700CCBY, 2018.
- 485 Carlson, W. D.: Scales of disequilibrium and rates of equilibration during metamorphism, *American Mineralogist*, 87(2–3), 185–204, doi:10.2138/am-2002-2-301, 2002.
- Cisneros, M. and Befus, K.: Applications and limitations of elastic thermobarometry: insights from elastic modeling of inclusion-host pairs and example case studies, *Geochemistry, Geophysics, Geosystems*, accepted, doi:10.1029/2020GC009231, 2020.
- 490 Cisneros, M., Ashley, K. T. and Bodnar, R. J.: Evaluation and application of the quartz-inclusions-in-epidote mineral barometer, *American Mineralogist*, 105(8), 1140–1151, doi:10.2138/am-2020-7379, 2020.



- Cooperdock, E. H. G. and Stockli, D. F.: Unraveling alteration histories in serpentinites and associated ultramafic rocks with magnetite (U-Th)/He geochronology, *Geology*, 44(11), 967–970, doi:10.1130/G38587.1, 2016.
- Dragovic, B., Samanta, L. M., Baxter, E. F. and Selverstone, J.: Using garnet to constrain the duration and rate of water-releasing metamorphic reactions during subduction: An example from Sifnos, Greece, *Chemical Geology*, 314–317, 9–22, doi:10.1016/j.chemgeo.2012.04.016, 2012.
- Dragovic, B., Baxter, E. F. and Caddick, M. J.: Pulsed dehydration and garnet growth during subduction revealed by zoned garnet geochronology and thermodynamic modeling, Sifnos, Greece, *Earth and Planetary Science Letters*, 413, 111–122, doi:10.1016/j.epsl.2014.12.024, 2015.
- Enami, M., Nishiyama, T. and Mouri, T.: Laser Raman microspectrometry of metamorphic quartz: A simple method for comparison of metamorphic pressures, *American Mineralogist*, 92(8–9), 1303–1315, doi:10.2138/am.2007.2438, 2007.
- Franz, G. and Liebscher, A.: Physical and Chemical Properties of the Epidote Minerals—An Introduction—, *Reviews in Mineralogy and Geochemistry*, 56(1), 1–81, doi:10.2138/gsrmg.56.1.1, 2004.
- Gatta, G. D., Merlini, M., Lee, Y. and Poli, S.: Behavior of epidote at high pressure and high temperature: a powder diffraction study up to 10 GPa and 1,200 K, *Phys Chem Minerals*, 38(6), 419–428, doi:10.1007/s00269-010-0415-y, 2011.
- Gautier, P., Brun, J.-P. and Jolivet, L.: Structure and kinematics of Upper Cenozoic extensional detachment on Naxos and Paros (Cyclades Islands, Greece), *Tectonics*, 12(5), 1180–1194, doi:10.1029/93TC01131, 1993.
- Grasemann, B., Schneider, D. A., Stöckli, D. F. and Iglseider, C.: Miocene bivergent crustal extension in the Aegean: Evidence from the western Cyclades (Greece), *Lithosphere*, 4(1), 23–39, doi:10.1130/L164.1, 2012.
- Grasemann, B., Huet, B., Schneider, D. A., Rice, A. H. N., Lemonnier, N. and Tschegg, C.: Miocene postorogenic extension of the Eocene synorogenic imbricated Hellenic subduction channel: New constraints from Milos (Cyclades, Greece), *GSA Bulletin*, 130(1–2), 238–262, doi:10.1130/B31731.1, 2018.
- Groppo, C., Forster, M., Lister, G. and Compagnoni, R.: Glaucophanite schists and associated rocks from Sifnos (Cyclades, Greece): New constraints on the P–T evolution from oxidized systems, *Lithos*, 109(3), 254–273, doi:10.1016/j.lithos.2008.10.005, 2009.
- Holland, T. and Powell, R.: An improved and extended internally consistent thermodynamic dataset for phases of petrological interest, involving a new equation of state for solids, *Journal of Metamorphic Geology*, 29(3), 333–383, doi:10.1111/j.1525-1314.2010.00923.x, 2011.
- Isaak, D. G., Anderson, O. L. and Oda, H.: High-temperature thermal expansion and elasticity of calcium-rich garnets, *Phys Chem Minerals*, 19(2), 106–120, doi:10.1007/BF00198608, 1992.
- Jamtveit, B., Austrheim, H. and Putnis, A.: Disequilibrium metamorphism of stressed lithosphere, *Earth-Science Reviews*, 154, 1–13, doi:10.1016/j.earscirev.2015.12.002, 2016.
- Javoy, M.: Stable isotopes and geothermometry, *Journal of the Geological Society*, 133(6), 609–636, doi:10.1144/gsjgs.133.6.0609, 1977.



- Jolivet, L. and Brun, J.-P.: Cenozoic geodynamic evolution of the Aegean, *Int J Earth Sci (Geol Rundsch)*, 99(1), 109–138, doi:10.1007/s00531-008-0366-4, 2010.
- Jolivet, L., Lecomte, E., Huet, B., Denèle, Y., Lacombe, O., Labrousse, L., Le Pourhiet, L. and Mehl, C.: The North Cycladic Detachment System, *Earth and Planetary Science Letters*, 289(1), 87–104, doi:10.1016/j.epsl.2009.10.032, 2010.
- 530 Keiter, M., Ballhaus, C. and Tomaschek, F.: A new geological map of the Island of Syros (Aegean Sea, Greece): implications for lithostratigraphy and structural history of the Cycladic Blueschist Unit, Geological Society of America., 2011.
- Kohn, M. J. and Spear, F.: Retrograde net transfer reaction insurance for pressure-temperature estimates, *Geology*, 28(12), 1127–1130, doi:10.1130/0091-7613(2000)28<1127:RNTRIF>2.0.CO;2, 2000.
- 535 Kotowski, A. J. and Behr, W. M.: Length scales and types of heterogeneities along the deep subduction interface: Insights from exhumed rocks on Syros Island, Greece, *Geosphere*, 15(4), 1038–1065, doi:10.1130/GES02037.1, 2019.
- Lagos, M., Scherer, E. E., Tomaschek, F., Münker, C., Keiter, M., Berndt, J. and Ballhaus, C.: High precision Lu–Hf geochronology of Eocene eclogite-facies rocks from Syros, Cyclades, Greece, *Chemical Geology*, 243(1), 16–35, doi:10.1016/j.chemgeo.2007.04.008, 2007.
- 540 Lanari, P. and Engi, M.: Local Bulk Composition Effects on Metamorphic Mineral Assemblages, *Reviews in Mineralogy and Geochemistry*, 83(1), 55–102, doi:10.2138/rmg.2017.83.3, 2017.
- Lanari, P., Giuntoli, F., Loury, C., Burn, M. and Engi, M.: An inverse modeling approach to obtain P–T conditions of metamorphic stages involving garnet growth and resorption, *European Journal of Mineralogy*, 29(2), 181–199, doi:10.1127/ejm/2017/0029-2597, 2017.
- 545 Laurent, V., Jolivet, L., Roche, V., Augier, R., Scaillet, S. and Cardello, G. L.: Strain localization in a fossilized subduction channel: Insights from the Cycladic Blueschist Unit (Syros, Greece), *Tectonophysics*, 672–673, 150–169, doi:10.1016/j.tecto.2016.01.036, 2016.
- Laurent, V., Lanari, P., Nair, I., Augier, R., Lahfid, A. and Jolivet, L.: Exhumation of eclogite and blueschist (Cyclades, Greece): Pressure–temperature evolution determined by thermobarometry and garnet equilibrium modelling, *Journal of*
- 550 *Metamorphic Geology*, 36(6), 769–798, doi:10.1111/jmg.12309, 2018.
- Liati, A. and Seidel, E.: Metamorphic evolution and geochemistry of kyanite eclogites in central Rhodope, northern Greece, *Contrib Mineral Petrol*, 123(3), 293–307, doi:10.1007/s004100050157, 1996.
- Lister, G. S. and Forster, M. A.: White mica $40\text{Ar}/39\text{Ar}$ age spectra and the timing of multiple episodes of high-P metamorphic mineral growth in the Cycladic eclogite–blueschist belt, Syros, Aegean Sea, Greece, *Journal of Metamorphic Geology*, 34(5),
- 555 401–421, doi:10.1111/jmg.12178, 2016.
- Matthews, A. and Schliestedt, M.: Evolution of the blueschist and greenschist facies rocks of Sifnos, Cyclades, Greece, *Contr. Mineral. and Petrol.*, 88(1), 150–163, doi:10.1007/BF00371419, 1984.
- Mazzucchelli, M. L., Burnley, P., Angel, R. J., Morganti, S., Domeneghetti, M. C., Nestola, F. and Alvaro, M.: Elastic geothermobarometry: Corrections for the geometry of the host-inclusion system, *Geology*, 46(3), 231–234,
- 560 doi:10.1130/G39807.1, 2018.



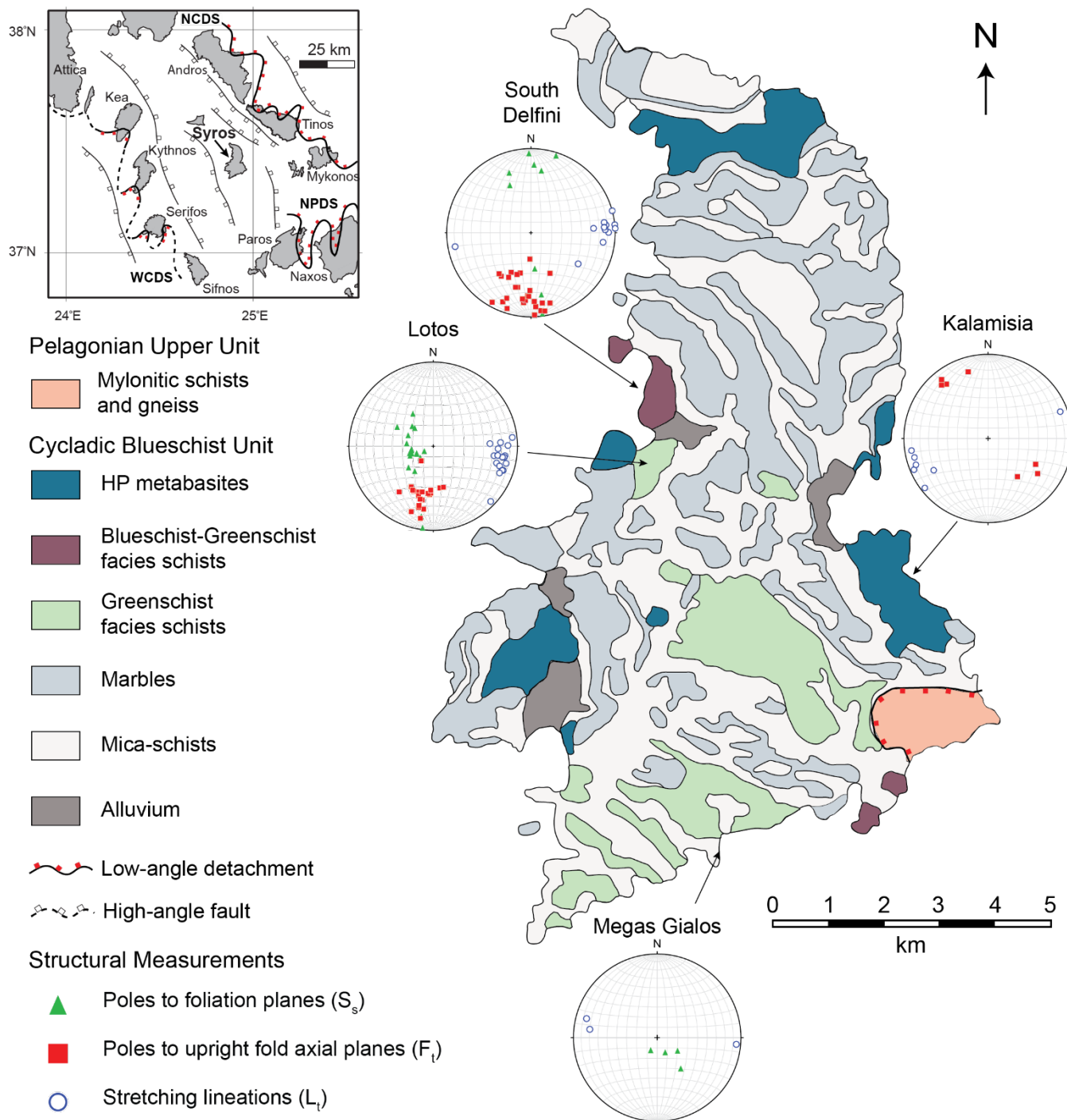
- Milani, S., Angel, R. J., Scandolo, L., Mazzucchelli, M. L., Ballaran, T. B., Klemme, S., Domeneghetti, M. C., Miletich, R., Scheidl, K. S., Derzsi, M., Tokár, K., Prencipe, M., Alvaro, M. and Nestola, F.: Thermo-elastic behavior of grossular garnet at high pressures and temperatures, *American Mineralogist*, 102(4), 851–859, doi:10.2138/am-2017-5855, 2017.
- Murri, M., Mazzucchelli, M. L., Campomenosi, N., Korsakov, A. V., Prencipe, M., Mihailova, B. D., Scambelluri, M., Angel, R. J. and Alvaro, M.: Raman elastic geobarometry for anisotropic mineral inclusions, *American Mineralogist*, 103(11), 1869–1872, doi:10.2138/am-2018-6625CCBY, 2018.
- Murri, M., Alvaro, M., Angel, R. J., Prencipe, M. and Mihailova, B. D.: The effects of non-hydrostatic stress on the structure and properties of alpha-quartz, *Phys Chem Minerals*, doi:10.1007/s00269-018-01018-6, 2019.
- Nye, J. F.: *Physical properties of crystals: their representation by tensors and matrices*, Oxford university press., 1985.
- Pawley, A. R., Redfern, S. A. T. and Holland, T. J. B.: Volume behavior of hydrous minerals at high pressure and temperature: I. Thermal expansion of lawsonite, zoisite, clinozoisite, and diaspore, *American Mineralogist*, 81(3–4), 335–340, doi:10.2138/am-1996-3-407, 1996.
- Peacock, S. M.: The importance of blueschist → eclogite dehydration reactions in subducting oceanic crust, *GSA Bulletin*, 105(5), 684–694, doi:10.1130/0016-7606(1993)105<0684:TIOBED>2.3.CO;2, 1993.
- Pe-Piper, G. and Piper, D. J. W.: *The igneous rocks of Greece: The anatomy of an orogen*, Beiträge zur Regionalen Geologie der Erde, Gebrüder Borntraeger, 2002.
- Powell, R. and Holland, T.: Optimal geothermometry and geobarometry, *American Mineralogist*, 79(1–2), 120–133, 1994.
- Qin, F., Wu, X., Wang, Y., Fan, D., Qin, S., Yang, K., Townsend, J. P. and Jacobsen, S. D.: High-pressure behavior of natural single-crystal epidote and clinozoisite up to 40 GPa, *Phys Chem Minerals*, 43(9), 649–659, doi:10.1007/s00269-016-0824-7, 2016.
- Ridley, J.: Evidence of a temperature-dependent ‘blueschist’ to ‘eclogite’ transformation in high-pressure metamorphism of metabasic rocks, *Journal of Petrology*, 25(4), 852–870, 1984.
- Ring, U., Glodny, J., Will, T. and Thomson, S.: The Hellenic Subduction System: High-Pressure Metamorphism, Exhumation, Normal Faulting, and Large-Scale Extension, *Annual Review of Earth and Planetary Sciences*, 38(1), 45–76, doi:10.1146/annurev.earth.050708.170910, 2010.
- Ring, U., Pantazides, H., Glodny, J. and Skelton, A.: Forced Return Flow Deep in the Subduction Channel, Syros, Greece, *Tectonics*, 39(1), e2019TC005768, doi:10.1029/2019TC005768, 2020.
- Rosenbaum, G., Avigad, D. and Sánchez-Gómez, M.: Coaxial flattening at deep levels of orogenic belts: evidence from blueschists and eclogites on Syros and Sifnos (Cyclades, Greece), *Journal of Structural Geology*, 24(9), 1451–1462, doi:10.1016/S0191-8141(01)00143-2, 2002.
- Rosenfeld, J. L.: Stress effects around quartz inclusions in almandine and the piezothermometry of coexisting aluminum silicates, *Am J Sci*, 267(3), 317–351, doi:10.2475/ajs.267.3.317, 1969.
- Rosenfeld, J. L. and Chase, A. B.: Pressure and temperature of crystallization from elastic effects around solid inclusions in minerals?, *Am J Sci*, 259(7), 519–541, doi:10.2475/ajs.259.7.519, 1961.



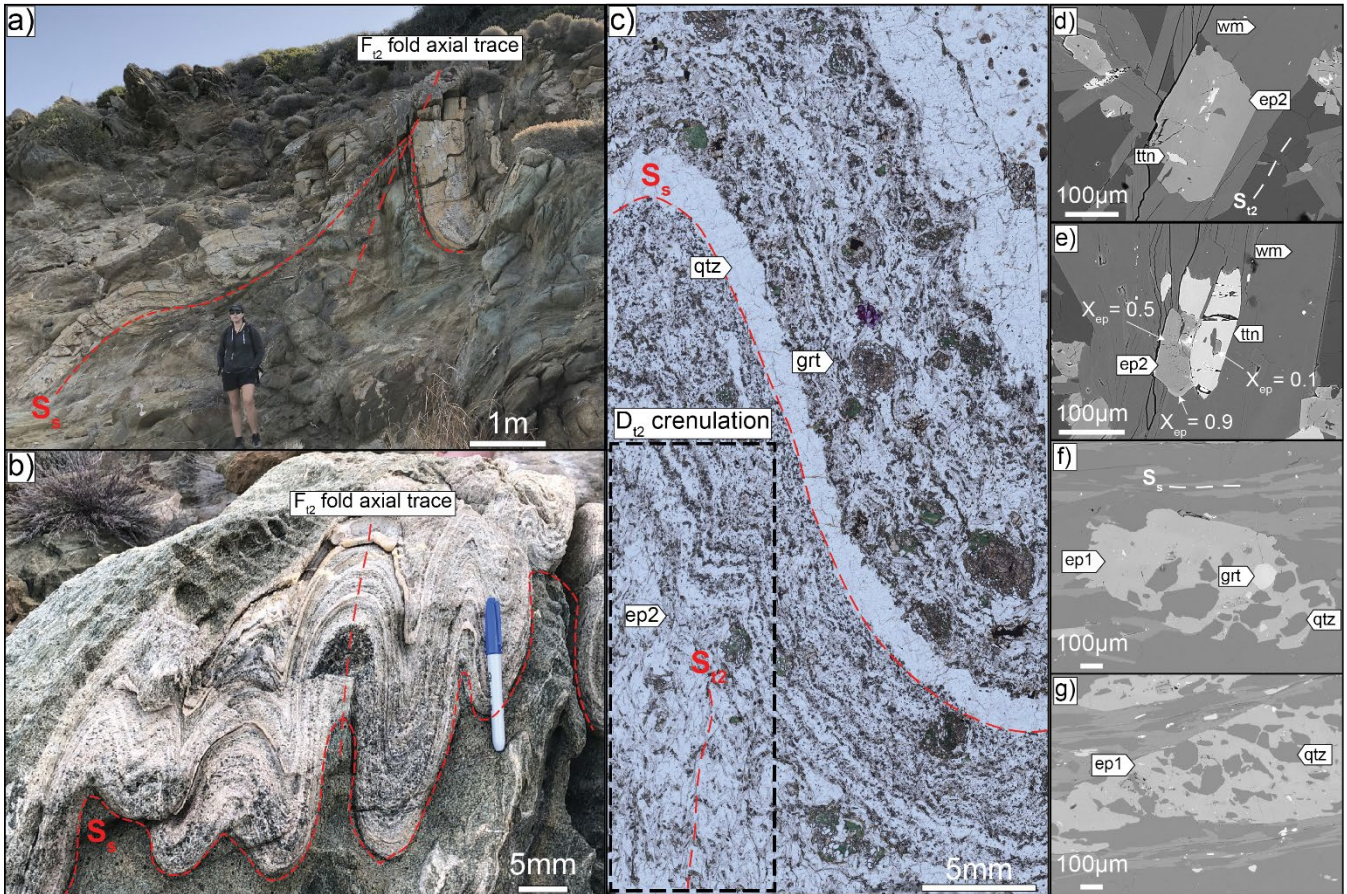
- 595 Rubie, D. C.: Disequilibrium during metamorphism: the role of nucleation kinetics, Geological Society, London, Special Publications, 138(1), 199–214, doi:10.1144/GSL.SP.1996.138.01.12, 1998.
- Schmädicke, E. and Will, T. M.: Pressure–temperature evolution of blueschist facies rocks from Sifnos, Greece, and implications for the exhumation of high-pressure rocks in the Central Aegean, *Journal of Metamorphic Geology*, 21(8), 799–811, doi:10.1046/j.1525-1314.2003.00482.x, 2003.
- 600 Schmidt, C. and Ziemann, M. A.: In-situ Raman spectroscopy of quartz: A pressure sensor for hydrothermal diamond-anvil cell experiments at elevated temperatures, *American Mineralogist*, 85(11–12), 1725–1734, doi:10.2138/am-2000-11-1216, 2000.
- Schneider, D. A., Grasemann, B., Lion, A., Soukis, K. and Draganits, E.: Geodynamic significance of the Santorini Detachment System (Cyclades, Greece), *Terra Nova*, 30(6), 414–422, doi:10.1111/ter.12357, 2018.
- 605 Schumacher, J. C., Brady, J. B., Cheney, J. T. and Tonnsen, R. R.: Glaucofane-bearing Marbles on Syros, Greece, *J Petrology*, 49(9), 1667–1686, doi:10.1093/petrology/egn042, 2008.
- Sharp, Z. D.: A laser-based microanalytical method for the in situ determination of oxygen isotope ratios of silicates and oxides, *Geochimica et Cosmochimica Acta*, 54(5), 1353–1357, doi:10.1016/0016-7037(90)90160-M, 1990.
- Sharp, Z. D. and Kirschner, D. L.: Quartz-calcite oxygen isotope thermometry: A calibration based on natural isotopic variations, *Geochimica et Cosmochimica Acta*, 58(20), 4491–4501, doi:10.1016/0016-7037(94)90350-6, 1994.
- 610 Skelton, A., Peillod, A., Glodny, J., Klonowska, I., Månbro, C., Lodin, K. and Ring, U.: Preservation of high-P rocks coupled to rock composition and the absence of metamorphic fluids, *Journal of Metamorphic Geology*, 0(0), doi:10.1111/jmg.12466, 2018.
- Spear, F. S. and Pattison, D. R. M.: The implications of overstepping for metamorphic assemblage diagrams (MADs), *Chemical Geology*, 457, 38–46, doi:10.1016/j.chemgeo.2017.03.011, 2017.
- 615 Spear, F. S. and Selverstone, J.: Quantitative P-T paths from zoned minerals: Theory and tectonic applications, *Contr. Mineral. and Petrol.*, 83(3), 348–357, doi:10.1007/BF00371203, 1983.
- Syracuse, E. M., van Keken, P. E. and Abers, G. A.: The global range of subduction zone thermal models, *Physics of the Earth and Planetary Interiors*, 183(1), 73–90, doi:10.1016/j.pepi.2010.02.004, 2010.
- 620 Thomas, J. B. and Spear, F. S.: Experimental study of quartz inclusions in garnet at pressures up to 3.0 GPa: evaluating validity of the quartz-in-garnet inclusion elastic thermobarometer, *Contrib Mineral Petrol*, 173(5), 42, doi:10.1007/s00410-018-1469-y, 2018.
- Trotet, F., Vidal, O. and Jolivet, L.: Exhumation of Syros and Sifnos metamorphic rocks (Cyclades, Greece). New constraints on the P-T paths, *European Journal of Mineralogy*, 13(5), 901–902, doi:10.1127/0935-1221/2001/0013-0901, 2001a.
- 625 Trotet, F., Jolivet, L. and Vidal, O.: Tectono-metamorphic evolution of Syros and Sifnos islands (Cyclades, Greece), *Tectonophysics*, 338(2), 179–206, doi:10.1016/S0040-1951(01)00138-X, 2001b.
- Urey, H. C.: The thermodynamic properties of isotopic substances, *Journal of the Chemical Society (Resumed)*, 562–581, 1947.



- 630 Walowski, K. J., Wallace, P. J., Hauri, E. H., Wada, I. and Clynne, M. A.: Slab melting beneath the Cascade Arc driven by
dehydration of altered oceanic peridotite, *Nature Geoscience*, 8(5), 404–408, doi:10.1038/ngeo2417, 2015.
- Wang, J., Mao, Z., Jiang, F. and Duffy, T. S.: Elasticity of single-crystal quartz to 10 GPa, *Phys Chem Minerals*, 42(3), 203–
212, doi:10.1007/s00269-014-0711-z, 2015.
- Wang, Z. and Ji, S.: Elasticity of six polycrystalline silicate garnets at pressure up to 3.0 GPa, *American Mineralogist*, 86(10),
1209–1218, doi:10.2138/am-2001-1009, 2001.
- 635 Zhong, X., Moulas, E. and Tajčmanová, L.: Post-entrapment modification of residual inclusion pressure and its implications
for Raman elastic thermobarometry, *Solid Earth*, 11(1), 223–240, doi:<https://doi.org/10.5194/se-11-223-2020>, 2020.



640 **Figure 1.** Geologic map of Syros, Greece [modified from Keiter et al. (2011) and Behr et al. (2018)]. Inset map shows Syros relative to the North and West Cycladic, and Naxos-Paros Detachment Systems (NCSD, WCDS, NPDS, modified from Grasemann et al., 2012). Stereonets from each studied outcrop are shown, and arrows indicate the outcrop location.



645 Figure 2. Outcrop, micrograph, and electron images showing stages of retrograde deformation present in southern Delfini. a) Upright folds (F_{12}) that refold the primary S_s foliation. b): Core of F_{12} folds (below Fig. 2a, KCS34). c): Plane light image of sample KCS34; sample cut perpendicular to the F_{12} fold axial plane. Epidotes (ep2) from the upright fold exhibit recrystallization as indicated by alignment with a late S_{12} crenulation, and a reduction in inclusions and grain size. d) Ep2 with late titanite (ttn) inclusions. Ep2 is parallel to white mica (wm) that defines S_{12} (KCS34). e) Ep2 in textural equilibrium with ttn (KCS34). f) Ep1 parallel to S_s , with garnet (grt) and quartz (qtz) inclusions that do not define an internal foliation (KCS1621). g) Poikiloblastic ep1 parallel to S_s , with a weak internal foliation defined by qtz (KCS1621).
650
655
660

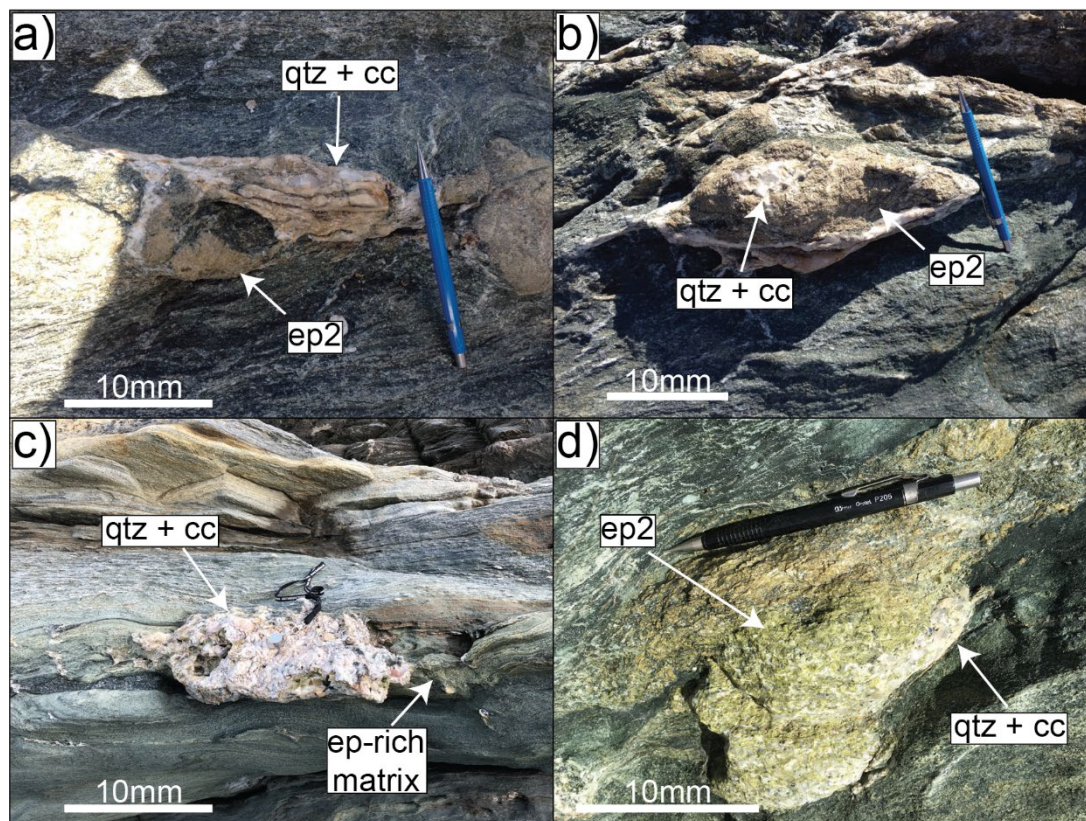
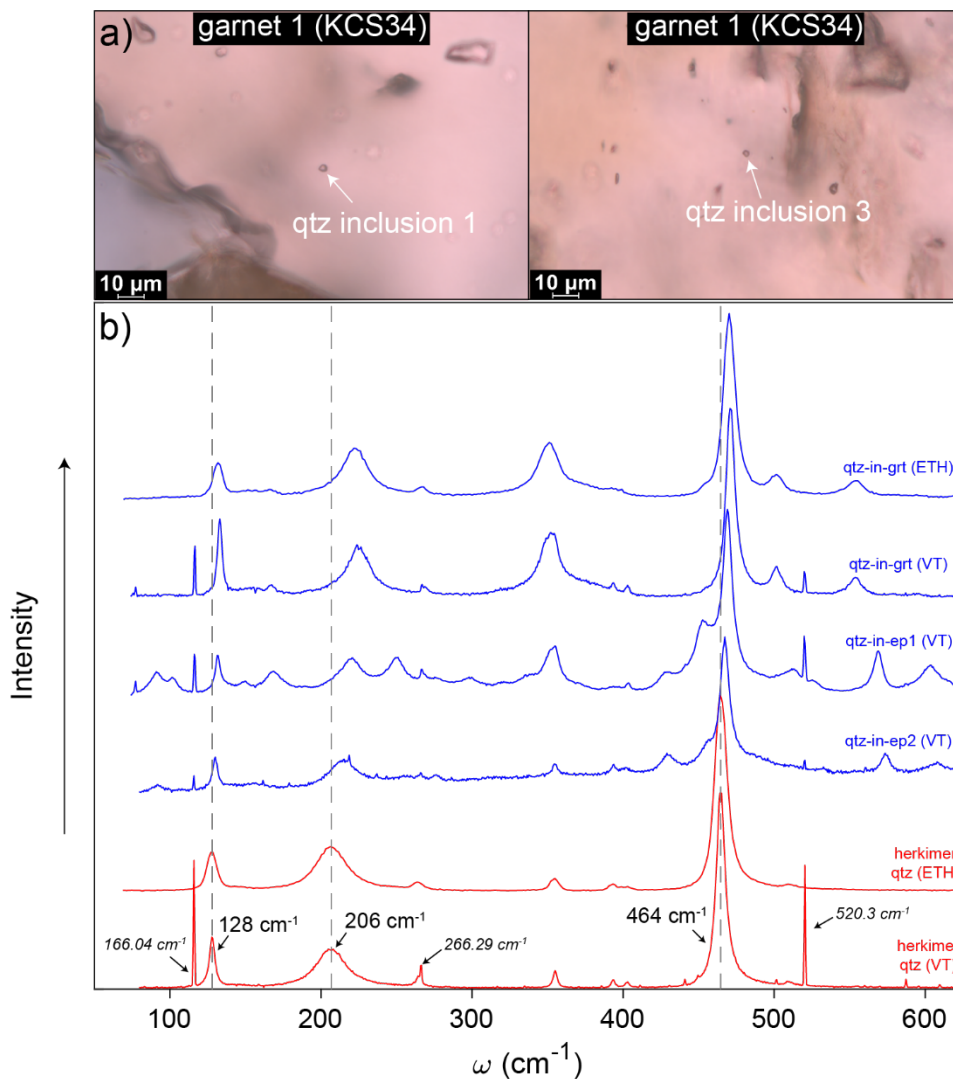
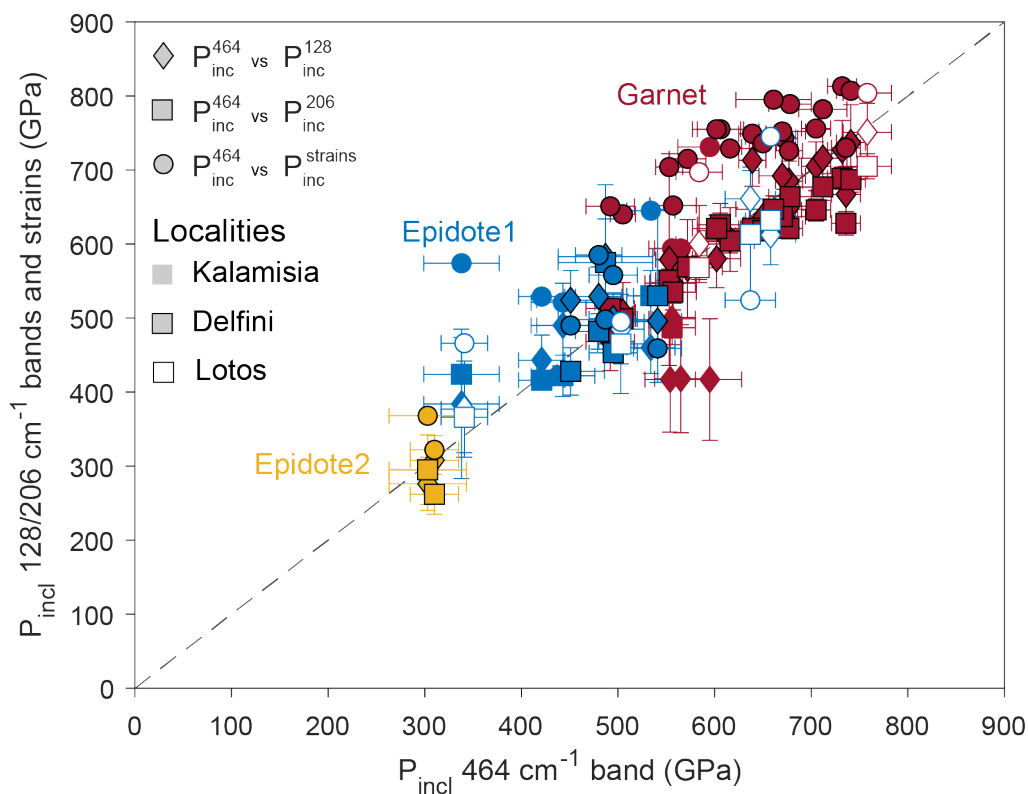


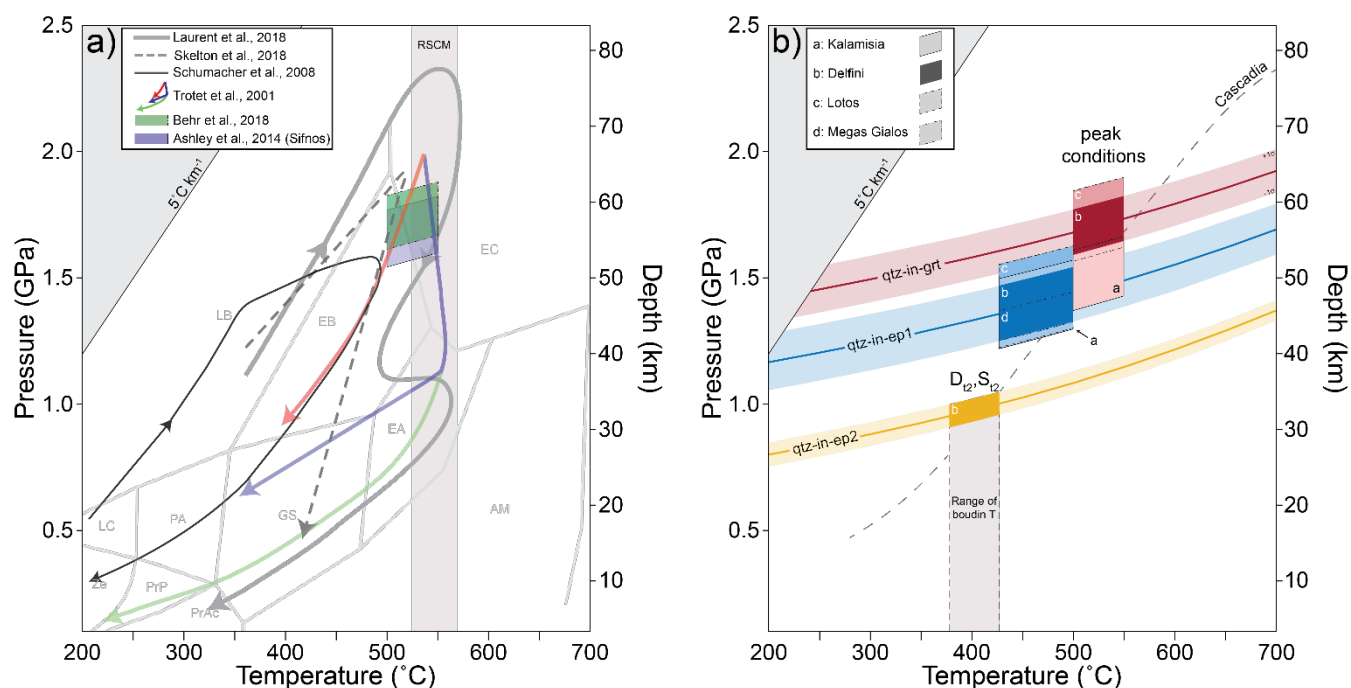
Figure 3. Outcrop photos of epidote boudins sampled for oxygen isotope thermometry. a) SY1613 (Lotos), b) SY1617 (Delfini), c) SY1618 (Delfini), d) SY1623 (Delfini).



665 **Figure 4. Photomicrographs of measured quartz inclusions in garnet from Delfini (a) and Raman spectrums of unstrained Herkimer quartz and strained quartz inclusions (b). b) Shown for comparison are Herkimer quartz (red) and quartz inclusion (blue) measurements from Virginia Tech and ETH Zürich. Quartz bands and Ar plasma lines (only VT analyses) are numerically labelled.**



670 **Figure 5.** Comparison of P_{inc} determined from different quartz bands using hydrostatic calibrations, and by using phonon-mode Grüneisen tensors (strains). Red, blue, and yellow symbols indicate qtz-in-grt (Group), qtz-in-ep1 (Group 2), and qtz-in-ep2 (Group 3) results, respectively. Diamonds, squares, and circles indicate P_{inc}^{464} vs P_{inc}^{128} , P_{inc}^{464} vs P_{inc}^{206} , and P_{inc}^{464} vs $P_{inc}^{strains}$ results, respectively. No border, filled, and open symbols indicate analyses from Kalamisia, Delfini, and Lotos samples, respectively.



675 Figure 6. (a) Reference P-T conditions and (b) P-T conditions deduced from elastic thermobarometry and oxygen isotope
 thermometry superimposed on modeled Cascadia slab-top geotherm (Syracuse et al., 2010). a) Recalculated P_{trap} values from Behr
 et al. (2018) (Syros) and Ashley et al. (2014) (Sifnos) and are shown in blue and red rectangles, respectively. Metamorphic facies
 are taken from (Peacock, 1993). b) P_{trap} from Groups 1, 2, and 3, that reflect peak (qtz-in-garnet), retrograde blueschist-greenschist
 680 facies (qtz-in-ep1), and late greenschist facies (qtz-in-ep2) conditions. Solid red, blue, and yellow lines and rectangles are the P_{trap}
 isomekes (calculated from the mean residual inclusion pressure of each group) and our best-estimate entrapment conditions,
 respectively. Transparent lines are P_{trap} errors (1σ around the mean) for analyses from Delfini samples. Grey box bounds the range
 of temperatures calculated from oxygen isotope thermometry of quartz-calcite boudin neck precipitates. Metamorphic facies fields
 (Peacock, 1993): zeolite (ZE), prehnite-pumpellyite (PrP), prehnite-actinolite (PrAc), pumpellyite-actinolite (PA), lawsonite-chlorite
 (LC), greenschist (GS), lawsonite-blueschist (LB), epidote-blueschist (EB), epidote-amphibolite (EA), amphibolite (AM), eclogite
 (EC). RSCM = Raman Spectroscopy of Carbonaceous Material (data from Laurent et al., 2018).

685